Journal of Materials Chemistry C

ROYAL SOCIETY OF CHEMISTRY

PAPER

View Article Online
View Journal

Cite this: DOI: 10.1039/d3tc00496a

Manipulating the sublattice distortion induced by Mn^{2+} doping for boosting the emission characteristics of self-trapped excitons in Cs_4SnBr_6†

Zhenxu Lin, [a] Anyang Wang, [c] Rui Huang,*[b] Haixia Wu,[b] Jie Song,[b] Zewen Lin,[b] Dejian Hou, [b] Zhaofu Zhang, [d] Yuzheng Guo *[c] and Sheng Lan*[a]

The fundamental photophysics involved in the doping effect of zero-dimensional (0D) lead-free tin-halide perovskites (Cs_4SnX_6, X = Br and I), especially the dynamics of self-trapped excitons (STEs), is crucial for their practical applications. Here, we proposed the use of Mn^{2+} doping to realize efficient emission from the STEs in Cs_4SnBr_6. The Mn^{2+}-doped Cs_4SnBr_6 exhibits an enhanced photoluminescence (PL) quantum yield of up to ~75.8%, a broadened emission spectrum, and improved thermal stability. The experimental observations combined with first-principles calculations reveal that the significant PL enhancement originates from the enhanced electron–phonon coupling and the increased binding energies of STEs, as a consequence of the large distortion of $[SnBr_6]^{4-}$ octahedra induced by Mn^{2+} doping. In addition, it was verified that the color tuning of Mn^{2+}-doped Cs_4SnBr_6 is achieved by the competitive transfers of free excitons to STE states and Mn^{2+} sites based on time-resolved and temperature-dependent PL measurements. The Mn^{2+}-doped Cs_4SnBr_6 assembled into commercial UV-LED chips exhibits strong white light emission with a color temperature of 6346 K. Our findings not only provide deep insight into the dynamics of STEs in Mn^{2+}-doped Cs_4SnBr_6 but also open new horizons for manipulating and optimizing the emission of STEs in 0D perovskites, thereby laying a foundation for developing white LEDs based on 0D perovskites.

Received 11th February 2023,
Accepted 3rd April 2023

DOI: 10.1039/d3tc00496a

rsc.li/materials-c

Introduction

Lead metal halide perovskite ($CsPbX_3$, X = Cl, Br, and I) quantum dots (QDs) have been widely used in the fabrication of phosphor-converted white light-emitting diodes (LEDs) due to their high photoluminescence (PL) quantum yields (QY) and widely tunable emissions.[1–4] However, the practical applications of $CsPbX_3$ QDs are hindered by the toxicity of Pb and limited PL QYs caused by the self-absorption of multicomponents. Therefore, the development of environmentally friendly perovskite phosphors with high PL QYs and negligible self-absorption, which remains a big challenge, is highly desirable for white LEDs. Recently, it was found that zero-dimensional (0D) lead-free metal halide perovskites, which possess soft lattice and structural confinement, exhibit broadband light emission with a large Stokes shift and high PL QYs from self-trapped excitons (STEs).[5–8] Among them, 0D tin halide perovskites (Cs_4SnX_6, X = Br and I) emerged as promising materials for environmental friendly phosphors with high PL QYs because of their similar electronic structures to those of lead halide perovskites.[9–14] Kovalenko's group reported fully inorganic 0D Cs_4SnBr_6 showing strong green emission from STEs with a PL QY of 15% ± 5%.[10] Unfortunately, the stability of Cs_4SnBr_6 is influenced by the oxidation of Sn^{2+}, limiting its practical applications. Very recently, Cs_4SnBr_6 with long-term stability and a high PL QY of 62.8% was successfully fabricated by Zhang and coauthors through introduction of F^- into Cs_4SnBr_6 to suppress the oxidation of Sn^{2+}.[14] From the practical application in white LEDs, the emission efficiency and thermal stability of Cs_4SnBr_6 need to be further improved while its emission spectrum needs to be broadened.

In general, the emission from free excitons (FEs), which are formed through the spatial confinement, features a narrow band with the PL peak located near the optical absorption onset. In contrast, the emission of STEs shows a broad PL band with a large Stokes shift due to the excited-state electron–hole

[a] Guangdong Provincial Key Laboratory of Nanophotonic Functional Materials and Devices, School of Information and Optoelectronic Science and Engineering, South China Normal University, Guangzhou 510006, China. E-mail: slan@scnu.edu.cn
[b] School of Material Science and Engineering, Hanshan Normal University, Chaozhou 521041, China. E-mail: rhuang@hstc.edu.cn
[c] School of Electrical Engineering and Automation, Wuhan University, Wuhan, 430072, China. E-mail: yguo@whu.edu.cn
[d] The Institute of Technological Sciences, Wuhan University, Wuhan, 430072, China

† Electronic supplementary information (ESI) available. See DOI: https://doi.org/10.1039/d3tc00496a

pairs captured through strong electron–phonon coupling to lattice distortion.[15–17] The properties of STEs depend profoundly on the octahedral distortion. This feature offers us the opportunity to achieve desired optical properties by regulating structural distortions. For example, a large distortion in $[PbBr_6]^{4-}$ octahedra was induced through high-pressure structural modulation, which significantly boosted the emission of STEs from 0D Cs_4PbBr_6.[18] In fact, it is well known that metal ion doping in all-inorganic perovskites is useful for modifying their optical and electronic properties.[19–21] However, STEs can hardly be obtained in 3D all-inorganic perovskites with cubic phase crystal structures, in spite of the size mismatch between the dopant and substituted atoms. The main obstacle is the difficulty of lattice distortion in 3D perovskites because octahedrons are firmly connected with each other through vertices. Fortunately, the low crystal dimensionality of 0D perovskites facilitates octahedral distortion and thus the formation of STEs because of the independent inorganic framework.[22–24] In 0D perovskites, B-site substitution with ions of different radii could engender the deviation of ionic radius in favor of producing largely distorted $[BX_6]^{4-}$ octahedra, thus strengthening electron phonon coupling.[25–27] Therefore, the impurity doping in 0D halide perovskites is expected to provide an alternative strategy to regulate the emission of STEs. Nevertheless, the fundamental photophysics involved in the doping of 0D perovskites, especially the dynamics of STEs, remains unexplored.

In this article, we proposed the use of Mn^{2+} doping to enhance the emission of STEs in lead-free Cs_4SnBr_6. The influence of Mn^{2+} doping on the electronic structure and optical properties of Cs_4SnBr_6 was systematically investigated. It was found that Mn^{2+}-doped Cs_4SnBr_6 exhibits enhanced PL QYs of up to ~75.8%, which is attributed to the enhanced electron–phonon coupling and the increased binding energies of STEs originating from the large distortion of $[SnBr_6]^{4-}$ octahedra induced by Mn^{2+} doping. Furthermore, the color tuning in the PL can be achieved by the competitive transfers of FE to STE states and Mn^{2+} sites. By exploiting the high PL QYs and excellent thermal stability of Mn^{2+}-doped Cs_4SnBr_6, we revealed their great potential as efficient yellowish-green phosphors for application in UV-converted white LEDs.

Results and discussion

In Fig. 1(a), we show schematically the synthesis of Mn^{2+}-doped Cs_4SnBr_6 with different molar ratios of Mn^{2+} (x = 0, 0.5, 1, and 2) by using water-assisted ball-milling at room temperature (see left panel). The images of four samples, which are denoted as S-0, S-0.5, S-1, and S-2, under the illumination of UV light are also provided (see right panel). It is noticed that the emission color of Cs_4SnBr_6 is changed from green (S-0) to orange (S-2) when the molar ratio of Mn^{2+} is increased from 0 to 2. In Fig. 1(b), we present the normalized PL spectra measured for different samples. Sample S-0 features a broadband emission peak at ~530 nm. In addition, it exhibits a large Stokes shift of ~1.29 eV, a long radiative lifetime of ~821 ns, and a high exciton binding energy of ~265 meV, as shown in Fig. S1 (ESI†). The full width at half maximum (FWHM) of the emission band was as large as ~104 nm. These are the unique features of STEs caused by Jahn–Teller distortion of $[SnBr_6]^{4-}$ octahedra in 0D perovskites.[14,28,29] In addition, the PL intensity of sample S-0 exhibits a linear relationship with the laser power ranging from 126 to 2816 nW. Therefore, green light with a broadband emitted from sample S-0 is attributed to radiative recombination of STEs (*i.e.*, the radiative transition from the STE state to the ground state).The PL QY of sample S-0 was measured to be ~66.4% (see Fig. S2, ESI†), similar to the value reported previously.[14] From Fig. 1(b), it is interesting to find that the PL QY of sample S-0.5 is increased to ~75.8%. To the best of our knowledge, this is the highest value obtained for Cs_4SnBr_6 (Table S1, ESI†).[9–14] With an increasing doping level, the PL band of sample S-1 is broadened with a small shoulder appearing ~590 nm, leading to the change in the emission color (see Fig. 1(a)). It was found that the PL at ~590 nm exhibited a nearly single exponential decay with a long lifetime of ~4.8 ms (see Fig. S3, ESI†). This behavior is quite similar to that reported in Mn^{2+}-doped $CsPbCl_3$ QDs, where the PL originates from the $^4T_1 \rightarrow {}^6A_1$ transition of Mn^{2+}.[30] In sample S-2, the PL spectrum is further broadened and dominated by the orange emission at ~590 nm. However, the PL QY dropped dramatically to ~45.6%.

In Fig. 1(c), we shown the XRD patterns obtained for different samples. The XRD pattern of S-0 shows the coexistent phase of Cs_4SnBr_6 and CsBr (the precursors are not consumed completely in the solid-state reaction). In addition to these diffraction peaks such as the strongest diffraction peak at 29.7° attributed to the CsBr phase, it can be seen that the diffraction peaks of S-0 from the Cs_4SnBr_6 phase is consistent with that reported for Cs_4SnBr_6-SnF_2, where the oxidation of Sn^{2+} in Cs_4SnBr_6 is suppressed by the substitution of Br^- with smaller F^-.[14] Moreover, the significantly decreased diffraction intensity at 29.7° after the addition of $MnBr_2$ indicated that $MnBr_2$ can effectively improve the efficiency of powder transformation. It was noticed that the XRD peak (*e.g.*, at 30.5°) is gradually shifted to a larger angle with increasing doping level. This behavior can be attributed to the substitution of Sn^{2+} by smaller Mn^{2+}.[19,31] The chemical compositions of Mn^{2+}-doped Cs_4SnBr_6 were examined by the elemental mapping of EDS, as shown in Fig. 1(d)–(i) (see Table S2, ESI†). It can be seen that the elements Cs, Sn, Mn, Br, and F are uniformly distributed over the Cs_4SnBr_6 crystal. Moreover, a remarkable increase of Mn^{2+}/Sn^{2+} from 0/9 to 15.1/4.12 was observed when the molar ratio was increased from 0 to 2, clearly indicating that more Sn^{2+} ions were replaced by Mn^{2+} with smaller sizes. As shown in Fig. 2(a), the Sn-Br bond length is 3.03 Å in Cs_4SnBr_6. When Sn^{2+} is substituted with Mn^{2+}, the bond length between Mn and its six adjacent Br is shortened to 2.75 Å, as shown in Fig. 2(d). The 9.2% decrease in bond length from $SnBr_6$ to $MnBr_6$ leads to two octahedra. This isostructural difference between $MnBr_6$ and $SnBr_6$ octahedra would result in a more significant asymmetry compared with pure Cs_4SnBr_6, which gives rise to a severe distortion of $[SnBr_6]^{4-}$ octahedra.

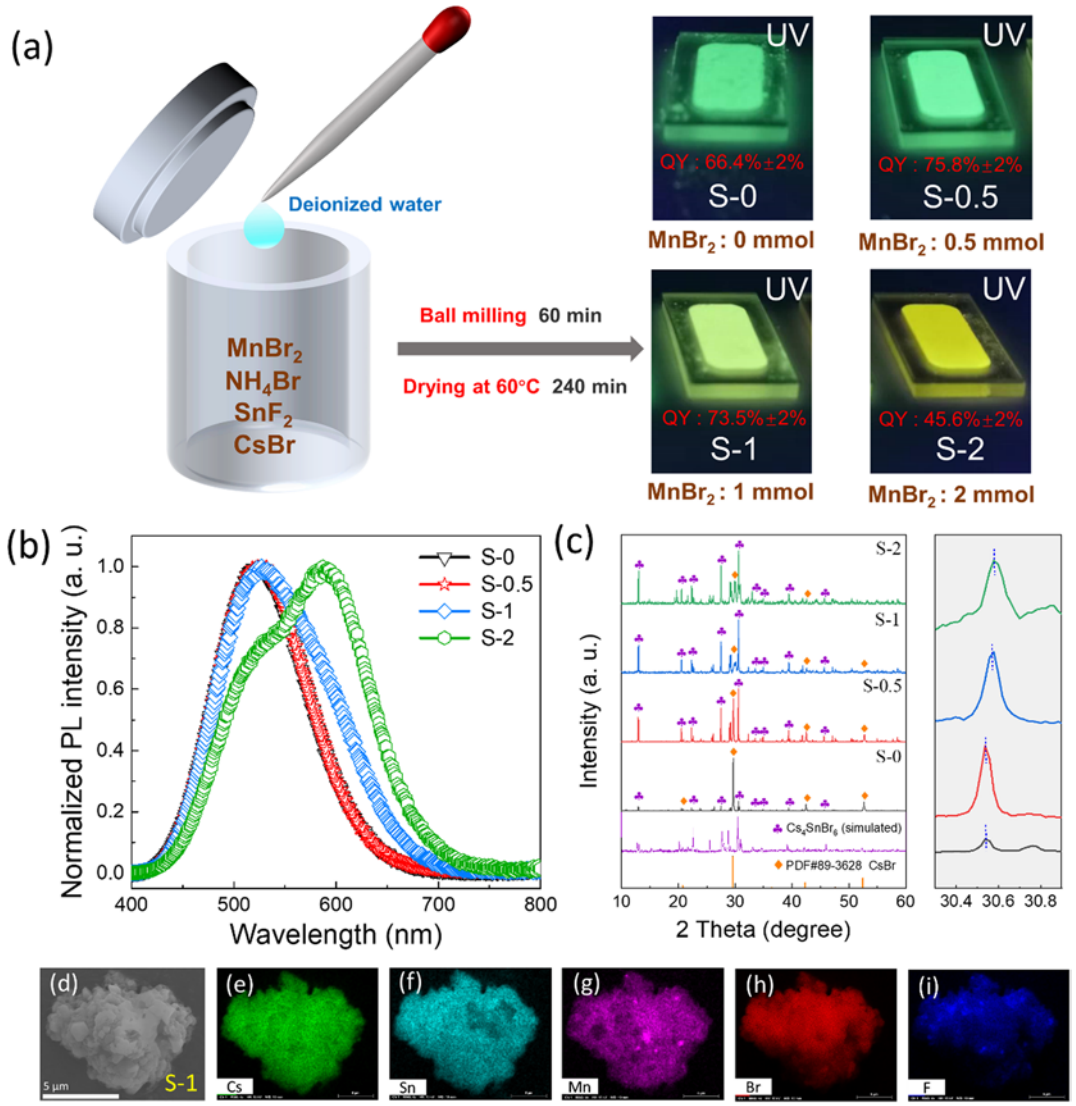

Fig. 1 (a) Schematic showing the method for synthesizing Mn^{2+}-doped Cs_4SnBr_6 (left panel). Deionized water is added in the powder mixture of CsBr, SnF_2, and NH_4Br with the $MnBr_2/SnF_2$ molar ratio of 0 : 1, 0.5 : 1, 1 : 1, and 2 : 1, respectively. Optical images of Mn^{2+}-doped Cs4SnBr6 with different doping levels illuminated by a 365 nm UV lamp with a power of 8 W. (b) Normalized PL spectra measured for Mn^{2+}-doped samples with different doping levels. (c) XRD patterns obtained for Mn^{2+}-doped samples with different doping levels compared with the simulated pattern of Cs_4SnBr_6 (labeled as clubs) and the pattern of CsBr (labeled as diamonds). (d) SEM image of a typical Mn^{2+}-doped Cs_4SnBr_6 powder (sample S-1). (e)–(i) EDS elemental maps of Cs, Sn, Mn, Br, and F in the Cs_4SnBr_6 powder shown in (d).

To gain more insight into the effects of Mn^{2+} doping, the electronic band structure of a typical Cs_4SnBr_6 supercell with and without Mn^{2+} doping were calculated with DFT, respectively, as shown in Fig. 2. Note that the valence band maximum of the band structures is set to 0 eV. It is found that the Cs_4SnBr_6 supercell with and without Mn^{2+} doping have almost the same band gap value ($\sim$3.4 eV), which is close to the measured value of 3.3 eV from Cs_4SnBr_6 with a low Mn^{2+} doping level based on the Kubelka–Munk transformed diffuse reflectance spectra displayed in Fig. S4 (ESI†).[32] However, the density of states in the conduction band and valence band significantly increase after Mn^{2+} doping. Furthermore, the Mn^{2+} doping induces occupied states lying at $\sim$0.2 eV above the valence band maximum (VBM) and unoccupied states lying at 0.11 eV below the conduction band minimum (CBM). The DOS in Fig. 2(f) shows that these shallow defect states originate from the Mn dopants. As demonstrated by Atta-Fynn *et al.*, the localized states stemming from defects would cause an anomalously large electron–phonon coupling.[33] The shallow defect states produced by the Mn^{2+} doping is expected to promoting the electron–phonon coupling. In fact, the increase in the density of energy states would improve light absorption and generate more electron–hole pairs, which is for beneficial for the enhancement of the electron–phonon coupling and the density of the photo-generated STEs in $Cs_4(Sn/Mn)Br_6$, boosting the emission of STEs.

In order to evaluate the influence of electron–phonon coupling, the temperature-dependent PL spectra of the samples

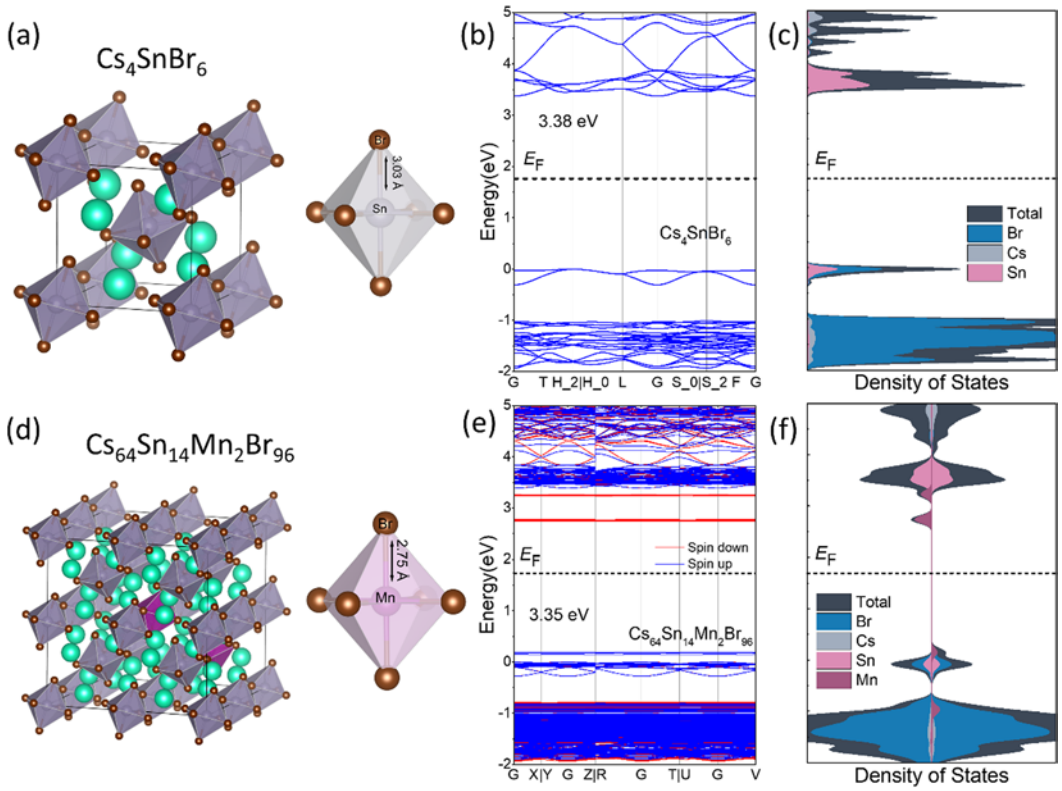

Fig. 2 Crystal structures, electronic band structures and DOS plots of Cs_4SnBr_6 (a–c) and $Cs_{64}Sn_{14}Mn_2Br_{96}$ (d–f), respectively. Note that the VBM of the band structures is set to 0 eV.

were measured in the range of 80 to 300 K. As shown in Fig. 3(a) and (b), an increase in the PL intensity as well as a reduction in the linewidth (FWHM) was observed with decreasing temperature for sample S-0.5. According to the theory of Toyozawa,[20] the temperature-dependent FWHM for the emission of STEs can be expressed as follows:

$$\mathrm{FWHM}(T) = 2.36\sqrt{S}\hbar\omega\sqrt{\coth\frac{\hbar\omega}{2k_{\mathrm{B}}T}}, \qquad (1)$$

where S is the Huang–Rhys factor, $\hbar\omega$ is the energy of the phonon mode, and k_{B} is Boltzmann's constant. As shown in Fig. 3(b) and Fig. S5 (ESI†), the value of Huang–Rhys factor S, which is often used to describe the exciton–phonon coupling, is increased from 41.2 to 49.5 by Mn^{2+} doping with a molar ratio of 0.5. The increase of S value indicates an enhancement in the electron–phonon coupling, which is more favorable for the formation of STEs and accounts for the broader emission band of STE. From the fitting in Fig. 3(b), the optical phonon energy

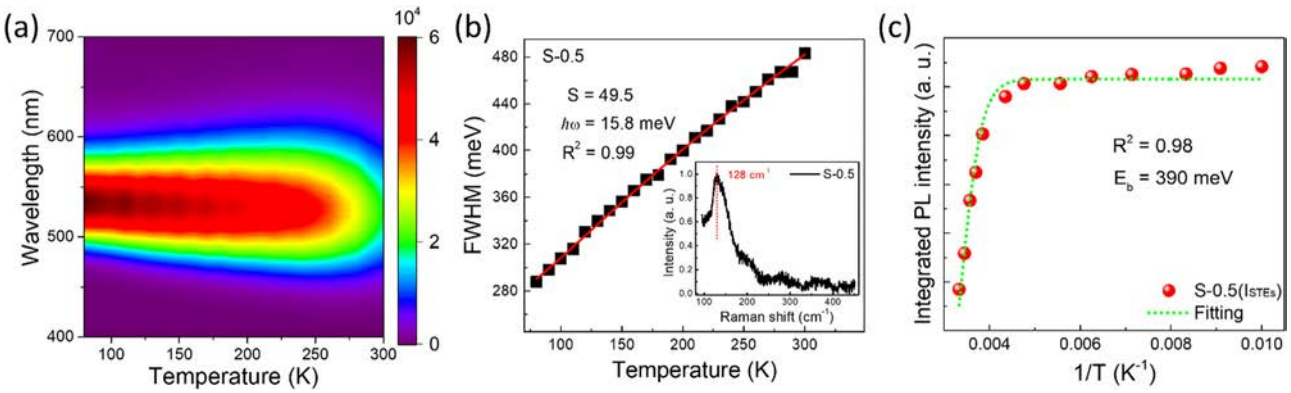

Fig. 3 (a) PL spectra of sample S-0.5 measured at different temperatures. (b) Temperature-dependent PL linewidth observed for sample S-0.5 (solid symbols) and the fitting of the experimental data (red line) by using eqn (1). The inset shows the Raman spectrum of sample S-0.5. (c) Integrated PL intensities of STEs based on deconvolution results for sample S-0.5 at different temperatures (red solid symbols). Also shown is the fitting of the experimental data (green dashed curve).

(E_{LO}) is extracted to be 15.8 meV (127 cm^{-1}), which is in good agreement with the Sn–Br stretching vibrational mode observed near 130 cm^{-1} in Cs_4SnBr_6 (see the inset of Fig. 3(b)).[34,35] It indicates that a dominant phonon mode corresponding to Sn-Br stretching vibrational mode is involved in the electron–phonon coupling. On the other hand, the PL QY of STEs relies strongly on the exciton binding energy because the detrapping of STEs by thermal activation will result in a lower radiative recombination rate. Basically, the exciton binding energy of STEs can be extracted from the temperature-dependent integrated PL intensity $I_{PL}(T)$ described by the Arrhenius equation:[36,37]

$$I_{PL}(T) = \frac{I_{PL}(T_0)}{1 + \beta \exp(-E_b/k_B T)}, \quad (2)$$

where I_{PL} (T_0) is the integrated PL intensity at 80 K, β is a constant related to the density of radiative recombination centers, k_B is Boltzmann's constant, and E_b is the exciton binding energy. By fitting the temperature-dependent integrated PL intensity of I_{STEs} with the Arrhenius equation, the exciton binding energy E_b can be derived empirically to be 390 meV and 334 meV for sample S-0.5 and sample S-1, respectively (see Fig. 3(c) and Fig. S6, ESI†). It is apparent that the value of E_b in Mn^{2+}-doped samples is greatly enhanced with respect to that (265 meV) in the undoped sample. It implies that the detrapping of STEs by thermal activation in Mn^{2+}-doped samples is effectively suppressed, leading to the enhancement in the emission from STEs. Thus, it is suggested that the enhanced electron–phonon coupling and the increased exciton binding energy induced by Mn^{2+} doping are suggested to be responsible for the enhanced emission from STEs observed in Mn^{2+}-doped samples.

It is noticed that with increasing doping levels, the PL band of sample S-2 is broadened and redshifted to ~590 nm with increasing doping level (see Fig. 1(c)). To gain a deep insight into the color tuning of PL observed for Mn^{2+}-doped Cs_4SnBr_6, we examined the excitation spectra of the Cs_4SnBr_6 host material (I_{STEs}) and Mn^{2+}-related emission ($I_{Mn^{2+}}$) in sample S-2, which are centered at 530 and 590 nm, respectively. It was found that excitation spectra of I_{STEs} and I_{Mn} possess nearly the same spectral shape, as shown in Fig. 4(a). It suggests that I_{STEs} and $I_{Mn^{2+}}$ originate from the relaxed excitons from the same excited state due to the s → p transition in Sn^{2+}. In Fig. 4(b), we compare the lifetime of I_{STEs} and I_{Mn} in sample S-2. The PL

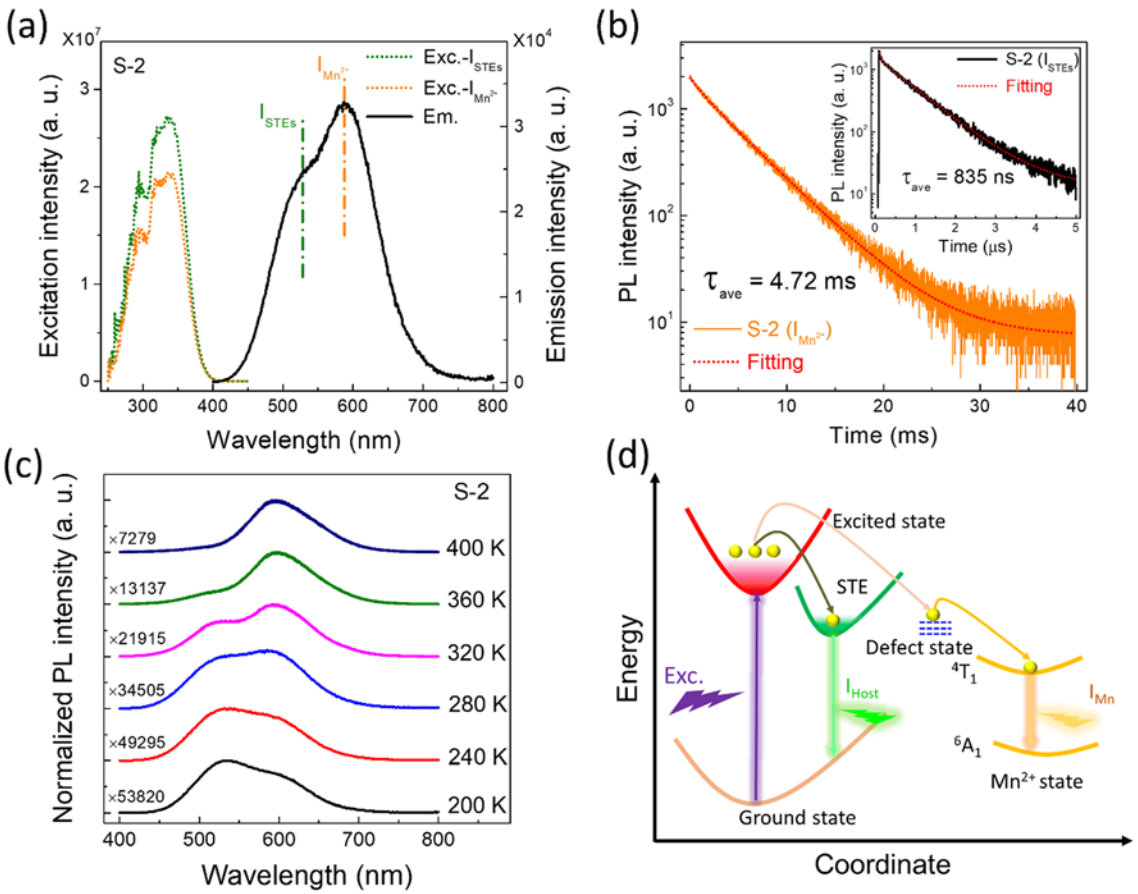

Fig. 4 (a) Excitation spectra measured for sample S-2 at the peak wavelengths of I_{STEs} (530 nm) and $I_{Mn^{2+}}$ (590 nm). The emission spectrum is also provided for reference. (b) Time-resolved PL decay trace of I_{Mn} recorded at 590 nm in sample S-2. The time-resolved PL decay trace of I_{STEs} recorded at 530 nm is shown in the inset. (c) Normalized PL spectra measured for sample S-2 at different temperatures. (d) Schematic energy band diagram illustrating the competitive transfer of FEs to the STE state and the Mn^{2+} state, which leads to the dual-color emission in Mn^{2+}-doped Cs_4SnBr_6.

decay trace of I_{Mn} was fitted by a biexponential function and the average lifetime was derived to be ~4.72 ms. This value is five orders of magnitude longer than that of I_{STEs}, which was found to be ~835 ns. These observations suggest the existence of a competitive relationship between I_{STEs} and I_{Mn} in sample S-2, as schematically illustrated in Fig. 4(d). Upon light excitation, the excitons lifted from the ground state to the excited state relax rapidly either to the STE state or to the Mn^{2+} state. In fact, it has been demonstrated that the transfer time from the excited state to STEs (~several ps) much faster than the transfer time from the excited state to the Mn^{2+} state (~several hundreds of ps).[38,39] As such, Mn^{2+} doping should not appear to influence the emission of STEs. Actually, it is found that the Mn^{2+} doping results in the formation of defect states in the mid-gap of Cs_4SnBr_6, as shown by the electronic band structure in Fig. 2(e). Previously, it was found that the transfer time from the excited state to such defect states is around several to tens of ps, enabling exciton trapping in the defect states is more competitive than STEs.[39] Therefore, in our case we think that upon light excitation excitons transfer to the doped Mn^{2+} state mediated by such intermediate defect states, and eventually give rise to the Mn^{2+} emission, as shown in Fig. 4(d). At a low doping level, the substitution of Sn^{2+} by Mn^{2+} breaks the inversion symmetry of the lattice and increases the lattice distortion of $[SnBr_6]^{4-}$ octahedra, leading to an enhanced emission from STEs. The increasing Mn^{2+} doping level results in the high density of defect states, which lead to a more efficient exciton trapping. Thus, the emission from sample S-2 becomes dominated by the orange emission (*i.e.*, I_{Mn}). This is further confirmed by the evolution of PL with temperatures shown in Fig. 4(c), where the orange PL from sample S-2 becomes completely dominated by the emission from I_{Mn} for temperatures higher than 360 K due to the antithermal quenching of the Mn^{2+} emission. In contrast, the PL spectrum of sample S-0.5 dominated by the emission from the STE state remains nearly unchanged even at 400 K (see Fig. S7, ESI†). On the other hand, the large substitution of Sn^{2+} by Mn^{2+} would result in the formation of Mn-rich domains, which deteriorates the original Cs_4SnBr_6 structure and creates more nonradiative recombination centers. This is the physical origin of why the PL QY is reduced in the samples with high doping levels.

Apart from outstanding PL properties, the Mn^{2+}-doped samples also exhibit excellent thermal stability. Usually, incorporation of transition metals with ionic radii smaller than Pb^{2+} can improve the thermal stability of lead halide perovskite because of the enhanced formation energy.[19] In Fig. 5(a) and Fig. S8 (ESI†), we show the temperature-dependent PL intensity observed for all samples in a heating/cooling cycle up to 125 °C. For sample S-0, a reduction in the PL intensity close to ~80% was observed after the heating/cooling cycle. It is usually ascribed to the agglomeration of powder in the heating process. In sharp contrast, the PL intensities of the three Mn^{2+}-doped samples remain 90%, 95%, and 80% of their original value at the end of the same heating/cooling cycle. For sample S-1, it exhibited a good thermal stability after three heating/cooling cycles even though the maximum heating temperature was

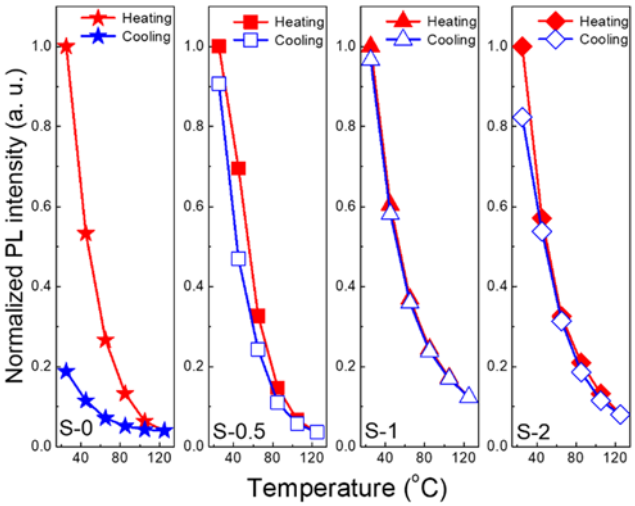

Fig. 5 Temperature-dependent PL intensity observed for the four samples with different doping levels in a heating/cooling cycle up to 125 °C.

increased to 165 °C, as shown in Fig. S9 (ESI†). It was also found that the thermal quenching of the emission from STEs appeared at a higher temperature of ~80 °C for Mn^{2+}-doped samples due to the suppression of thermally activated nonradiative recombination and de-trapping of STEs. Therefore, the combination of high PL QY and good thermal stability makes Mn^{2+}-doped Cs_4SnBr_6 a promising material for UV-pumped white LEDs. As a demonstration, we fabricated a white LED by placing the mixture of Mn^{2+}-doped Cs_4SnBr_6 emitting green-orange light and BAM: Eu^{2+} emitting blue light on a commercial 365-nm UV-LED chip without using epoxy or silica encapsulation for protection. In Fig. 6(a), it can be seen that the as-prepared LED emitted strong white light with a correlated color temperature (CCT) of 6346 K at an injected current of 100 mA. As shown in Fig. S10 (ESI†), the emission intensity of the LED increased gradually with increasing injected current and reached ~5600 cd m^{-2} at an injected current of 180 mA, implying a potential application for indoor illumination. Moreover, the emission intensity of the LED keep stable operation for 300 min in air under UV light irradiation (100 mA), as shown in Fig. 6(b).

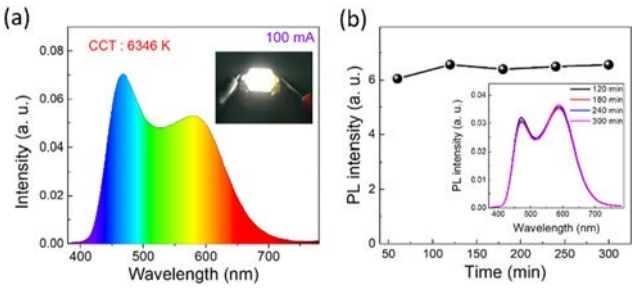

Fig. 6 (a) Emission spectrum and color temperature of the fabricated white LED at an injected current of 100 mA. The inset shows the photo of the LED at an injected current of 100 mA. (b) Integrated PL intensities of the LED under the continuous UV light illumination at different times. The inset shows the emission spectra of the LED measured at different times.

Conclusions

In summary, we have successfully enhanced the emission efficiency of STEs and broadened the emission spectra of Cs_4SnBr_6 through a Mn^{2+} doping strategy. It was found that Mn^{2+}-doped Cs_4SnBr_6 exhibited a dual-color emission, an enhanced PL QY of up to ~75.8%, and an improved thermal stability. Based on DFT calculations and temperature-dependent PL spectra, it was revealed that the enhanced emission from STEs originates from the enhanced electron–phonon coupling and the increased binding energy of STEs induced by the large distortion of $[SnBr_6]^{4-}$ octahedra by Mn^{2+} doping. Relying on the time-resolved and temperature-dependent PL measurements, it was confirmed that the competitive transfer of FEs to the STE state and the Mn^{2+} state is responsible for the color tuning from green to orange observed in Mn^{2+}-doped Cs_4SnBr_6. We demonstrated the potential application of Mn^{2+}-doped Cs_4SnBr_6 in white LEDs by fabricating an UV-pumped white LED with the mixture of Mn^{2+}-doped Cs_4SnBr_6 and BAM:Eu^{2+}, which exhibited strong white emission and good stability during a continuous operation time of 300 min. Our findings open new horizons for manipulating and optimizing the emission of STEs in 0D perovskites and pave the way for developing highly efficient white LEDs based on 0D perovskites.

Author contributions

R. Huang and S. Lan proposed the experimental design and revised paper; Z. Lin engineered the experiments and wrote the first draft of the manuscript; H. Wu, J. Song, Z. Lin, and D. Hou prepared the samples and performed the XRD characterization. A. Wang, Z. Zhang and Y. Guo conducted the first-principles calculations. All authors contributed to the analysis of data and general discussion.

Conflicts of interest

There are no conflicts to declare.

Acknowledgements

The authors acknowledge the financial support from the National Natural Science Foundation of China (Grant No. 11874020, 12174123 and 12104117), the Natural Science Foundation of Guangdong Province (2020A1515010432) and the Special Innovation Projects of Guangdong Provincial Department of Education (2020KTSCX076).

Notes and references

1 L. Protesescu, S. Yakunin, M. I. Bodnarchuk, F. Krieg, R. Caputo, C. H. Hendon, R. X. Yang, A. Walsh and M. V. Kovalenko, *Nano Lett.*, 2015, **15**, 3692.
2 X. Li, Y. Wu, S. Zhang, B. Cai, Y. Gu, J. Song and H. Zeng, *Adv. Funct. Mater.*, 2016, **26**, 2435.
3 K. Lin, J. Xing, L. N. Quan, F. P. G. de Arquer, X. Gong, J. Lu, L. Xie, W. Zhao, D. Zhang, C. Yan, W. Li, X. Liu, Y. Lu, J. Kirman, E. H. Sargent, Q. Xiong and Z. We, *Nature*, 2018, **562**, 245.
4 M. Liu, Q. Wan, H. Wang, F. Carulli, X. Sun, W. Zheng, L. Kong, Q. Zhang, C. Zhang, Q. Zhang, S. Brovelli and L. Li, *Nat. Photonics*, 2021, **15**, 379.
5 Y. Jing, Y. Liu, J. Zhao and Z. Xia, *J. Phys. Chem. Lett.*, 2019, **10**, 7439.
6 L. Lian, M. Zheng, W. Zhang, L. Yin, X. Du, P. Zhang, X. Zhang, J. Gao, D. Zhang, L. Gao, G. Niu, H. Song, R. Chen, X. Lan, J. Tang and J. Zhang, *Adv. Sci.*, 2020, **7**, 2000195.
7 M. Cong, Q. Zhang, B. Yang, J. Chen, J. Xiao, D. Zheng, T. Zheng, R. Zhang, G. Qing, C. Zhang and K. Han, *Nano Lett.*, 2021, **21**, 8671.
8 B. Su, J. Jin, Y. Peng, M. S. Molokeev, X. Yang and Z. Xia, *Adv. Opt. Mater.*, 2022, **10**, 2102619.
9 R. Chiara, Y. O. Ciftci, V. I. E. Queloz, M. K. Nazeeruddin, G. Grancini and L. Malavasi, *J. Phys. Chem. Lett.*, 2020, **11**, 618.
10 B. M. Benin, D. N. Dirin, V. Morad, M. Wörle, S. Yakunin, G. Rainò, O. Nazarenko, M. Fischer, I. Infante and M. V. Kovalenko, *Angew. Chem., Int. Ed.*, 2018, **57**, 11329.
11 X. Zhang, H. Wang, S. Wang, Y. Hu, X. Liu, Z. Shi, V. L. Colvin, S. Wang, W. W. Yu and Y. Zhang, *Inorg. Chem.*, 2019, **59**, 533.
12 L. Tan, W. Wang, Q. Li, Z. Luo, C. Zou, M. Tang, L. Zhang, J. He and Z. Quan, *Chem. Commun.*, 2020, **56**, 387.
13 K. Xu, Q. Wei, H. Wang, B. Yao, W. Zhou, R. Gao, H. Chen, H. Li, J. Wang and Z. Ning, *Nanoscale*, 2022, **14**, 2248.
14 Q. Zhang, S. Liu, M. He, W. Zheng, Q. Wan, M. Liu, X. Liao, W. Zhan, C. Yuan, J. Liu, H. Xie, X. Guo, L. Kong and L. Li, *Angew. Chem., Int. Ed.*, 2022, **61**, e202205463.
15 B. Yang and K. Han, *J. Phys. Chem. Lett.*, 2021, **12**, 8256.
16 S. Sun, M. Lu, X. Gao, Z. Shi, X. Bai, W. W. Yu and Y. Zhang, *Adv. Sci.*, 2021, **8**, 2102689.
17 J. Wei, H. Liao, L. Zhou, J. Luo, X. Wang and D. Kuang, *Sci. Adv.*, 2021, **7**, eabg3989.
18 Z. Ma, Z. Liu, S. Lu, L. Wang, X. Feng, D. Yang, K. Wang, G. Xiao, L. Zhang, S. Redfern and B. Zou, *Nat. Commun.*, 2018, **9**, 4506.
19 S. Zou, Y. Liu, J. Li, C. Liu, R. Feng, F. Jiang, Y. Li, J. Song, H. Zeng, M. Hong and X. Chen, *J. Am. Chem. Soc.*, 2017, **139**, 11443.
20 X. Cheng, Z. Xie, W. Zheng, R. Li, Z. Deng, D. Tu, X. Shang, J. Xu, Z. Gong, X. Li and X. Chen, *Adv. Sci.*, 2022, **9**, 2103724.
21 O. Stroyuk, O. Raievska, J. Hauch and C. Brabec, *Angew. Chem., Int. Ed.*, 2023, **135**, e202212668.
22 H. Luo, S. Guo, Y. Zhang, K. Bu, H. Lin, Y. Wang, Y. Yin, D. Zhang, S. Jin, W. Zhang, W. Yang, B. Ma and X. Lü, *Adv. Sci.*, 2021, **8**, 2100786.
23 S. Zou, C. Liu, R. Li, F. Jiang, X. Chen, Y. Liu and M. Hong, *Adv. Mater.*, 2019, **31**, 1900606.
24 W. Zhang, S. Thapa, Y. Sun, S. Norville, H. Zhu, P. Zhu, G. Wang and W. Qin, *Chem. Eng. J.*, 2021, **423**, 130186.

25 J. Luo, X. Wang, S. Li, J. Liu, Y. Guo, G. Niu, L. Yao, Y. Fu, L. Gao, Q. Dong, C. Zhao, M. Leng, F. Ma, W. Liang, L. Wang, S. Jin, J. Han, L. Zhang, J. Etheridge, J. Wang, Y. Yan, E. H. Sargent and J. Tang, *Nature*, 2018, **563**, 541.
26 P. Han, C. Luo, S. Yang, Y. Yang, W. Deng and K. Han, *Angew. Chem., Int. Ed.*, 2020, **132**, 12809.
27 X. Li, X. Gao, X. Zhang, X. Shen, M. Lu, J. Wu, Z. Shi, V. L. Colvin, J. Hu, X. Bai, W. Yu and Y. Zhang, *Adv. Sci.*, 2021, **8**, 2003334.
28 E. R. Dohner, A. Jaffe, L. R. Bradshaw and H. I. Karunadasa, *J. Am. Chem. Soc.*, 2014, **136**, 13154.
29 Q. Guo, X. Zhao, B. Song, J. Luo and J. Tang, *Adv. Mater.*, 2022, **34**, 2201008.
30 B. Su, G. Zhou, J. Huang, E. Song, A. Nag and Z. Xia, *Laser Photonics Rev.*, 2021, **15**, 2000334.
31 Q. Sun, S. Wang, C. Zhao, J. Leng, W. Tian and S. Jin, *J. Am. Chem. Soc.*, 2019, **141**, 20089.
32 Y. Zhang, R. Huang, H. Li, D. Hou, Z. Lin, J. Song, Y. Guo, H. Lin, C. Song, Z. Lin and J. Robertson, *Acta Mater.*, 2018, **155**, 214.
33 R. Atta-Fynn, P. Biswas and D. A. Drabold, *Phys. Rev. B: Condens. Matter Mater. Phys.*, 2004, **69**, 245204.
34 M. Kuok, L. Tan, Z. Shen, C. Huan and K. Mok, *Solid State Commun.*, 1996, **97**, 497.
35 Z. Qin, S. Dai, V. Hadjiev, C. Wang, L. Xie, Y. Ni, C. Wu, G. Yang, S. Chen, L. Deng, Q. Yu, G. Feng, Z. Wang and J. Bao, *Chem. Mater.*, 2019, **31**, 9098.
36 X. Wang, X. Zhang, S. Yan, H. Liu and Y. Zhang, *Angew. Chem., Int. Ed.*, 2022, **61**, e202210853.
37 M. Baranowski and P. Plochocka, *Adv. Energy Mater.*, 2020, **10**, 1903659.
38 V. Pinchetti, A. Anand, Q. A. Akkerman, D. Sciacca, M. Lorenzon, F. Meinardi, M. Fanciulli, L. Manna and S. Brovelli, *ACS Energy Lett.*, 2018, **4**, 85.
39 B. Su, M. S. Molokeev and Z. Xia, *J. Phys. Chem. Lett.*, 2020, **11**, 2510.

